



Article

Diurnal Variation in Cloud and Precipitation Characteristics in Summer over the Tibetan Plateau and Sichuan Basin

Bangjun Cao ^{1,2} , Xianyu Yang ^{1,*}, Boliang Li ¹, Yaqiong Lu ³ and Jun Wen ¹

¹ School of Atmospheric Science, Chengdu University of Information Technology, Chengdu 610225, China; caobj@cuit.edu.cn (B.C.); pakleung1997@gmail.com (B.L.); jwen@cuit.edu.cn (J.W.)

² Institute for Geophysics and Meteorology, University of Cologne, 50969 Cologne, Germany

³ Institute of Mountain Hazards and Environment, Chinese Academy of Sciences, Chengdu 610041, China; yaqiong@imde.ac.cn

* Correspondence: xyang@cuit.edu.cn; Tel.: +86-199-4082-6090

Abstract: The diurnal variation in precipitation and cloud parameters and their influencing factors during summer over the Tibetan Plateau (TP) and Sichuan Basin (SB) were investigated using the Hydro-Estimator satellite rainfall estimates, ground observations, and ERA5 dataset. The precipitation and cloud parameters show diurnal propagation over the SB during the mei-yu period in contrast to such parameters over the TP. The diurnal maximum precipitation from the Hydro-Estimator satellite and cloud ice and liquid water content (cloud LWC and IWC) from the ERA5 dataset are concentrated in the early evening, while their diurnal minimums manifest in the morning. Cloud LWC accounts for more than 60% of the total water during almost the entire diurnal cycle over the inner TP and SB during the mei-yu period. The IWC accounts for more than 60% of the total water in the late afternoon over the edge of the SB and TP. The cloud base height (CBH) above ground level (AGL), the lifting condensation level (LCL) AGL, and the zero degree level AGL are almost equal over the TP during the summer period. The zero degree level AGL over the SB is higher than that over the TP because the air temperature lapse rate over the TP is larger. The thickness of liquid water cloud over the SB is larger than that over the TP. The correlation analysis shows that the CBH AGL and LCL AGL over the TP are related to the dewpoint spread, but less so over the SB because of the stronger turbulence and lower air density over the TP than the SB. Convective available potential energy has a larger impact on precipitation over the TP than the SB. The cloud LWC makes a larger contribution to the precipitation over the SB than over the TP, which is related to the mean zonal wind and diurnal cycle of low-level winds. The precipitation at the edge of the TP and SB (i.e., the steep downstream slope) is largely influenced by the ice water contained within clouds owing to the convergence rising motion over the slopes.

Keywords: Tibetan Plateau; Sichuan Basin; steep slope; precipitation; cloud; diurnal variation



Citation: Cao, B.; Yang, X.; Li, B.; Lu, Y.; Wen, J. Diurnal Variation in Cloud and Precipitation Characteristics in Summer over the Tibetan Plateau and Sichuan Basin. *Remote Sens.* **2022**, *14*, 2711. <https://doi.org/10.3390/rs14112711>

Academic Editors: Jing Wei and Kai Qin

Received: 15 April 2022

Accepted: 30 May 2022

Published: 5 June 2022

Publisher's Note: MDPI stays neutral with regard to jurisdictional claims in published maps and institutional affiliations.



Copyright: © 2022 by the authors. Licensee MDPI, Basel, Switzerland. This article is an open access article distributed under the terms and conditions of the Creative Commons Attribution (CC BY) license (<https://creativecommons.org/licenses/by/4.0/>).

1. Introduction

The Tibetan Plateau (TP) (26°00′–39°47′N, 73°19′–104°47′E) is often referred to as ‘the roof of the world’ owing to its average elevation exceeding 4000 m, or ‘the Asian water tower’ [1] because several of Asia’s major rivers such as the Yangtze, Yellow, and Lancang originate from the region. The precipitation over the TP is important to these rivers, and the heat supply of the TP serves as an important energy source of the atmosphere [1–3]. The TP has also a profound impact on the precipitation over its surrounding and downstream areas [4–7]. The Sichuan Basin (SB) is a deep basin with an elevation on average 2500 m lower than that of the TP. Remote sensing and ground observations and modeling of the diurnal cycle of cloud and precipitation over the TP are important to understand the weather and climate processes over the TP and surrounding areas. Recently, the second (TIPEX2) and third (TIPEX3) Tibetan Plateau Atmospheric Experiments were carried out [8] and obtained large quantities of observational data from the TP to the SB, especially ground

radar observations of cloud and precipitation. These observational data and analysis provide a basis for further studies on the mechanisms of cloud and precipitation and the improvement of parameterization schemes for cloud and precipitation physical processes.

According to ground- and satellite-based observations as well as simulation results in previous research, the total precipitation is <400 mm during the entire summer (June–August) over the TP, which is smaller than that over the surrounding areas [9]. Moreover, the monthly averaged precipitation rate is $\sim 0.3 \text{ mm h}^{-1}$; the precipitation rate in precipitation events is $1\text{--}20 \text{ mm h}^{-1}$; the averaged daily precipitation is <15 mm over the TP [10,11]. The cloud top height usually exceeds 12 km above ground level (AGL), and sometimes exceeds 16 km AGL over the TP, mainly including mixed-phase and ice-phase processes, in which super-cold water may be contained [9–11]. The average cloud base height (CBH) during summer over the TP exceeds 1.5 km AGL, which is larger than that over the plains and SB.

The summer precipitation in China can be divided into two stages: the mei-yu period and the midsummer period [12–16]. Precipitation during summer shows an obvious diurnal cycle, peaking in the evening, with the greatest change occurring over the central TP [17–22]. The eastern foothills of the TP are dominated by nocturnal rainfall before midsummer [23]. The diurnal cycle of precipitation from the TP to downstream areas shows diurnal propagation during the pre-mei-yu period. However, this diurnal propagation from the TP to downstream areas disappears during midsummer. The zonal wind weakens from the pre-mei-yu period to midsummer. In addition, the precipitation over the valleys of the Himalaya mainly occurs from midnight to the sunrise [24]. High quantities of cloud cover occur mainly over the ridges and then move to the valleys. Convective activity mainly occurs at night over the valleys [10]. Turbulence and convective cloud over the TP develop more easily than in the surrounding areas because the air density is lower. A convective cloud develops after sunrise, reaching a maximum from late afternoon to early morning the following day, as does convective available potential energy (CAPE) [6,14]. The diurnal cycle in monsoonal flow, the sea–land breeze, boundary-layer flow, low-level jet, aerosols, and inertial oscillation in the mid-level horizontal wind field in the mid-troposphere ($\sim 500 \text{ hPa}$) are the key factors that influence the diurnal variation in precipitation over the EASM region [25–27].

Satellite precipitation observation can obtain the precipitation on a global scale, which is better than conventional measurements made by rain (and snow) gauges and surface-based weather radar observations. Many advanced satellite algorithms have been released that make use of infrared and passive microwave data, for example, the Precipitation Estimation from Remotely Sensed Information using Artificial Neural Networks–Climate Data Record (PERSIANN-CDR) [28], the Integrated Multi-Satellite Retrievals for GPM (IMERG) [29], the Tropical Rainfall Measuring Mission (TRMM) Multisatellite Precipitation Analysis (TMPA) [30], the Climate Prediction Center Morphing technique (CMORPH) [31], and the Hydro-Estimator (HE) Satellite Rainfall Estimates [32]. Mountainous regions represent a major challenge for these satellite data products. Over highly complex topography such as the Andes area, HE provides the most stable result, which could be associated with the best performance of HE on the development of precipitation from warmer and relatively lower clouds [33]. The HE with orographic correction to some extent captures the spatial distribution and timing of diurnal convective events over a mountainous region [34]. In addition, spatial distribution in cloud optical thickness and the cloud water path derived from satellite retrievals over the TP were closely associated with the increase in water-vapor transport flux divergence [35].

However, there is little research on the differences in the diurnal cycle of precipitation between HE satellite products and ground observations datasets, as well as the differences between the TP and SB. Moreover, the macroscopic properties of clouds such as cloud cover and cloud liquid or ice water content (LWC and IWC, respectively) and their relationships with surface thermal effects have received minimal attention. HE satellite products do not provide cloud microphysical parameters, while reanalysis data can provide cloud microphysical parameters. Therefore, it is a good choice to combine reanalysis data and

high-precision satellite data such as HE satellite products to analyze the distribution characteristics of cloud microphysical parameters over the TP and SB. Focusing on the diurnal cycle of cloud physical parameters, this paper seeks to answer the following questions on the basis of satellite, ground, and cloud radar observations and a reanalysis dataset: (1) What are the phase differences of water within clouds during the diurnal cycles over the TP and SB, and how do these change diurnally? (2) What are the possible mechanisms responsible for the phase differences of precipitation and cloud? Following this introduction and a description of the data (Section 2) and methods (Section 3) employed in this study, the diurnal variation in precipitation and cloud parameters (CBH AGL, cloud cover, cloud IWC and LWC) over the TP and SB using ECMWF Reanalysis v5 (ERA5) and the ground and HE are investigated in Section 4. Additionally, the relationships of the precipitation rate in HE, and cloud cover and cloud IWC and LWC from ERA5 with surface thermal effects are investigated. This research is important for addressing the bias of precipitation in the diurnal cycle during ground and satellite observations.

2. Data

2.1. Hydro-Estimator Satellite Rainfall Estimates

The rainfall rate data from Hydro-Estimator (HE) Satellite Rainfall Estimates covering June, July, and August 2014–2020 were used in this study. The HE rainfall rate estimates were produced using the data from NOAA's Geostationary Operational Environmental Satellites and also using available geostationary data over Europe, Africa, and Asia. The datasets were downloaded from ftp://ftp.star.nesdis.noaa.gov/pub/smcd/emb/f_f/hydroest/world/world/archive/ (accessed on 1 January 2022). The horizontal resolution of HE dataset is ~4 km, and the temporal resolution is 1 h. The HE dataset has been widely used in various studies [21–23]. HE provides the most stable result for several kinds of algorithms that combine infrared and passive microwave data over mountainous regions [32–34].

2.2. Ground Observational Data

The data from 50 ground meteorological observation sites belonging to the China Meteorological Administration were chosen, covering June, July, and August 2014–2020. Among them, 36 were located in the TP region and 14 in the SB region. The data included precipitation, air temperature at 2 m, humidity, and surface pressure, with a temporal resolution of 1 h, that were employed. Detailed station information is provided in Tables S1 and S2 in the Supporting Information. Additionally, the data from 12 radiosondes, including temperature, wind, pressure, and lifting condensation level (LCL) were chosen. The remaining observations were from TIPEX3 and a research program entitled 'The interaction between the earth and atmosphere of the TP and its influence on the weather and climate in the downstream' [4,7] (Figure 1). Cloud radar data, including CBH, cloud cover, and LWC (temporal resolution: 1 min), at the sites of Naqu (30.46°N, 90.59°E; 4730 m above mean sea level (MSL)), Yushu (33.01°N, 96.56°E; 3689 m MSL), and Linzhi (29.46°N, 94.44°E; 3326 m MSL), from July and August 2014–2020, were also used. The LWC was retrieved by using the cloud radar data with the equation $LWC = 3z^{0.5}$, where LWC is a power relationship with reflectivity z . For details about the cloud radar instrument and the cloud radar LWC retrievals, see [36,37]. The locations of the observation sites are shown in Figure 1.

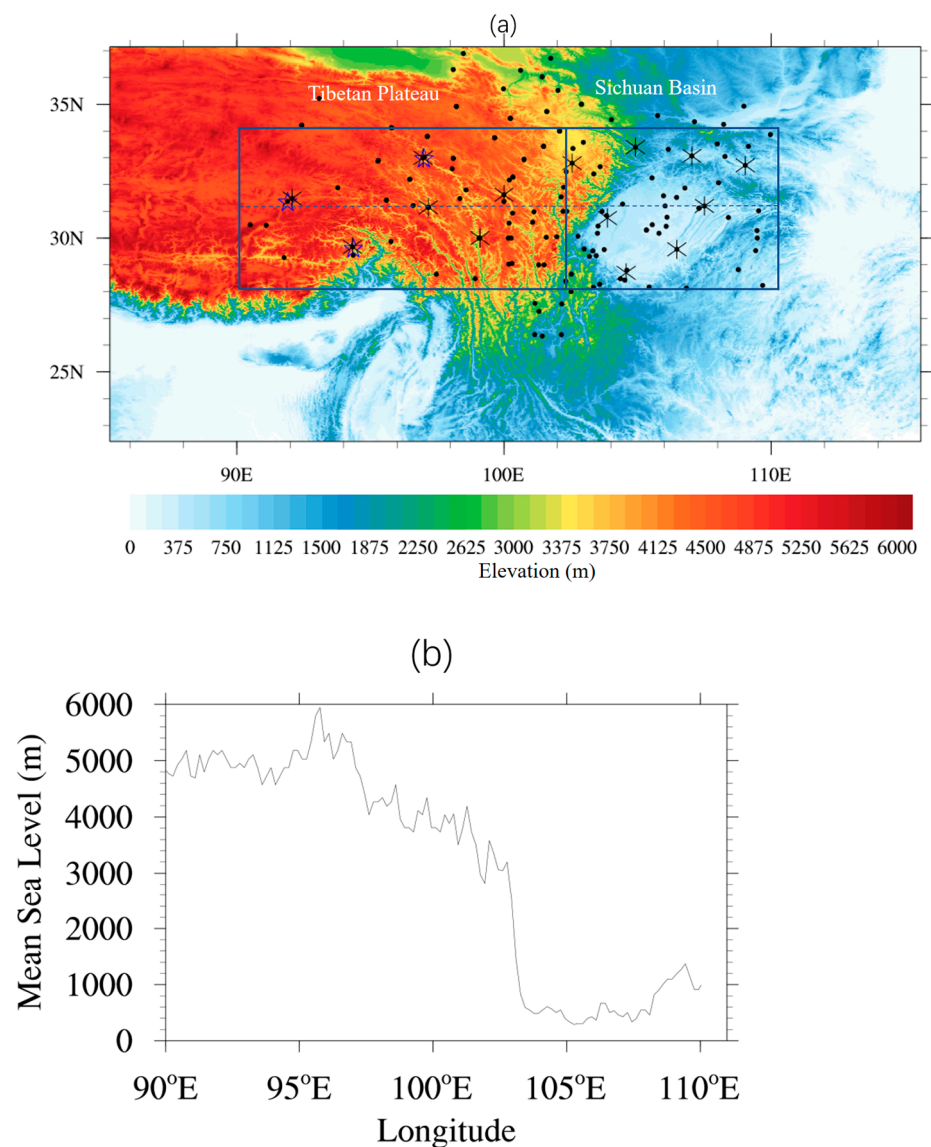


Figure 1. (a) Topography of the Tibetan Plateau and Sichuan Basin, in which the black dots indicate the locations of the ground meteorological observation sites of the China Meteorological Administration; ‘x’ represents the radiosonde stations; and pentagrams represent the cloud radar observation sites. (b) Elevation goes along the line of 31.2°N marked with the dashed blue line in (a).

2.3. ERA5 Reanalysis Dataset

We obtained hourly estimates of u-wind, v-wind, temperature, precipitation, CBH, cloud cover, cloud IWC, cloud LWC, dewpoint spread, zero degree level, and CAPE from the ERA5 reanalysis dataset. ERA5 combines vast amounts of historical observations into global estimates using advanced modeling and data assimilation systems. ERA5 has been widely used in various studies [38]. The ERA5 precipitation rate is greater than that in the observations when the precipitation rate is less than 10 mm day^{-1} over the TP [39]. The data were downloaded from <https://www.ecmwf.int/en/forecasts/datasets/reanalysis-datasets/era5> (accessed on 1 January 2022) and spanned the period 2014–2020 for the summer months of June, July, and August. The horizontal resolution of ERA5 is $\sim 31 \text{ km}$.

3. Methods

The summer precipitation in China can be divided into two stages: the mei-yu period and the midsummer period. The ‘mei-yu’ rain, also called plum rain or the East Asian rainy season, is caused by precipitation along a persistent stationary front known as the

Meiyu front for nearly two months during the late spring and early summer in East Asia. These weather systems can produce heavy rainfall and flooding. The typical mei-yu period is generally at the beginning of mid or late June and at the end of early or middle July [12–16]. Therefore, two time periods were chosen: (1) the mei-yu period, during 1–25 June in the monsoon phase and (2) the midsummer period, during 1 July–10 August. In terms of the study domain, the region of the eastern TP and its downstream area (28° – 34° N, 90° – 110° E) were chosen (Figure 1) [15], which were then further separated into two subregions with different elevations (framed areas in Figure 1): 90° – 100° E and 100° – 110° E, which represented the TP and SB. To describe the diurnal cycle during summer, the ERA5 and observational data were grouped into the mei-yu and midsummer seasons. The precipitation feature (PF) number is defined as the number of hours with precipitation in the diurnal cycle during the observational period when the precipitation observed was larger than 0.02 mm h^{-1} . The numbers of the PF in the two subregions during the two different seasons are listed in Table 1.

Table 1. The number of precipitation features (Unit: hour) from the Hydro-Estimator Satellite Rainfall Estimates dataset in the two subregions within 28° – 34° N shown in Figure 1 in each of the two chosen seasons.

	Tibetan Plateau	Sichuan Basin
Mei-yu	4531	2687
Midsummer	8145	3556

The ground and cloud radar observations were temporally averaged to 1 h. Local time (LT) was defined as Coordinated Universal Time (UTC) + 7 h. To match the ground observations with the satellite and ERA5 data in spatial terms, four grid values near the ground observations including precipitation and cloud parameters at different levels from the ERA5 dataset and satellite were interpolated using the bilinear interpolation method to produce the value at the ground observation site [40,41]. We use Hovmöller diagrams [23] to show the diurnal cycle of CBH, precipitation, dewpoint spread, IWC, and LWC and their changes with latitude. Typically, longitude is plotted along the x-axis, and time is recorded on the ordinate; then, the contour values of a named physical field are presented through color or shading. In addition, the height of the LCL can be calculated as $Z_{lcl} = 123(T - T_d)$, where T is the air temperature at 2 m, and T_d is the dewpoint temperature, in which the LCL is determined by the dewpoint spread.

4. Results

4.1. Diurnal Cycle of Precipitation and Cloud

During the mei-yu period, the diurnal variation in precipitation from HE satellite estimates shows phase propagation from west to east over the SB (103° – 110° E), while no such propagation can be seen over the TP (90° – 102° E) (Figure 2a), which is similar to the results of [23]. The diurnal maximum precipitation rate over the TP is concentrated between 1500 LT and 2100 LT, and the diurnal minimum precipitation rate lies within 0000–1200 LT. Over the SB, meanwhile, the diurnal maximum precipitation rate occurs at night, and then decreases to a minimum in the morning, which was also found in previous studies (e.g., [42]). The result for the PF number percentage is similar to that of the precipitation amount, except the maximum PF number percentage occurs at the boundary of the TP and SB (Figure 2c), which is related to the convergence rising motion over the slopes in the afternoon and rising motion in the center of the SB at night. During the midsummer period, the diurnal variation in the precipitation rate shows no propagation from the TP to SB, which is different from the mei-yu period. The diurnal maximum precipitation rate is concentrated between 1500 LT and 2100 LT, while the diurnal minimum precipitation rate lies within 0000–0600 LT, which is similar to that during the mei-yu period (Figure 2b). The average precipitation rate over the SB is larger than that over the TP. The result for the PF number percentage is similar to that of the precipitation amount (Figure 2d). The

reasons of the diurnal propagation of rainfall are related to the decreases in the zonal wind profile from the mei-yu to midsummer period and the diurnal cycle of low-level winds over the SB [23].

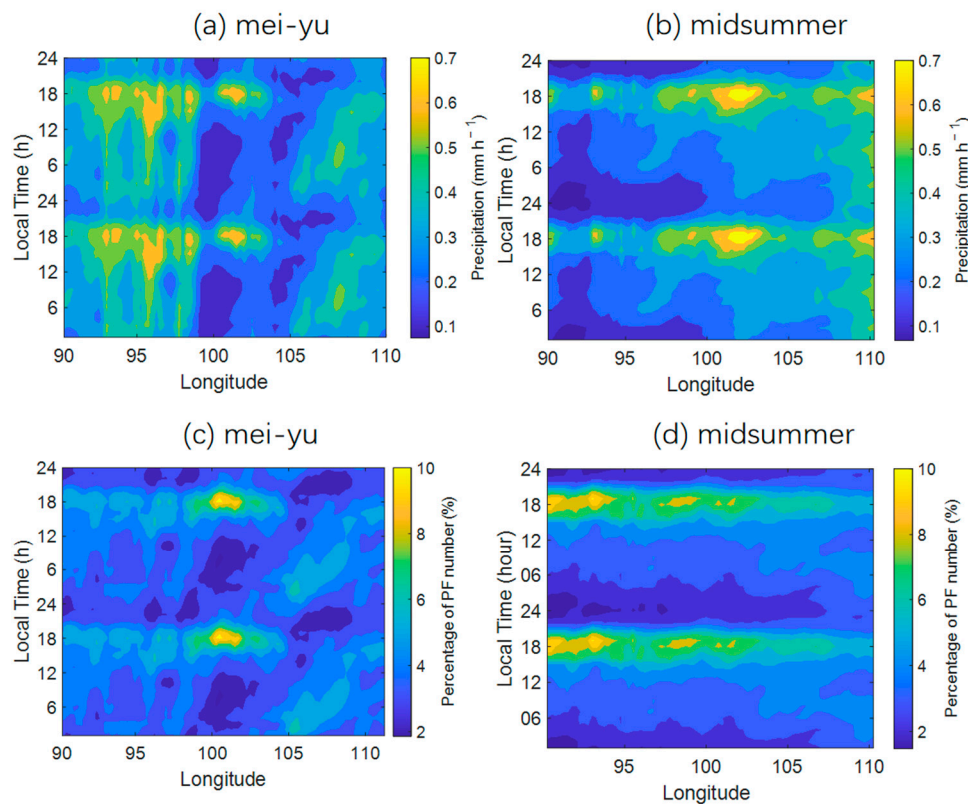


Figure 2. The (a,b) diurnal variation in precipitation and (c,d) precipitation feature number percentage during the (a,c) mei-yu and (b,d) midsummer period from the Hydro Estimator satellite rainfall estimates.

The precipitation from HE satellite estimates and ground observations are compared in Figure S1. Over the TP, the maximum precipitation rate from the HE satellite is 3 h ahead of that of the ground observations during the mei-yu and midsummer periods, and the precipitation rate from HE satellite is larger than that observed on the ground. Over the SB, the maximum precipitation rate from the HE satellite is also 3 h ahead of that of the ground observations during the mei-yu period, while it is in-phase with ground observations during the midsummer period. The result for the PF number percentage is comparable to that of the precipitation rate.

The diurnal variations in cloud cover, LWC, and IWC from ERA5 are shown in Figure 3. During the mei-yu period, the diurnal variation in cloud cover (Figure 3a), LWC (Figure 3c), and IWC (Figure 3e) shows propagation from west to east over the SB, while no diurnal propagation is apparent over the TP. The diurnal maximum cloud cover and LWC over the TP is concentrated between 1800 LT and 0300 LT, while over the SB they lie within 1500–2400 LT. The diurnal minimum cloud cover and LWC lie within 1000–1500 LT over both the TP and SB. The cloud cover and LWC at the border of the SB and TP are smaller than those over the inner parts of the two regions. The cloud cover and LWC in the SB are larger than those over the TP. The diurnal maximum IWC over the TP is concentrated between 1500 LT and 2100 LT, while the range for the diurnal minimum IWC is 0600–1200 LT. Over the SB, the diurnal maximum IWC is in the mid-afternoon to early evening (1500–2100 LT) and then decreases to a minimum during the morning (0600–1200 LT). The cloud IWC over the edge of TP and SB is larger than that over the inner TP and SB.

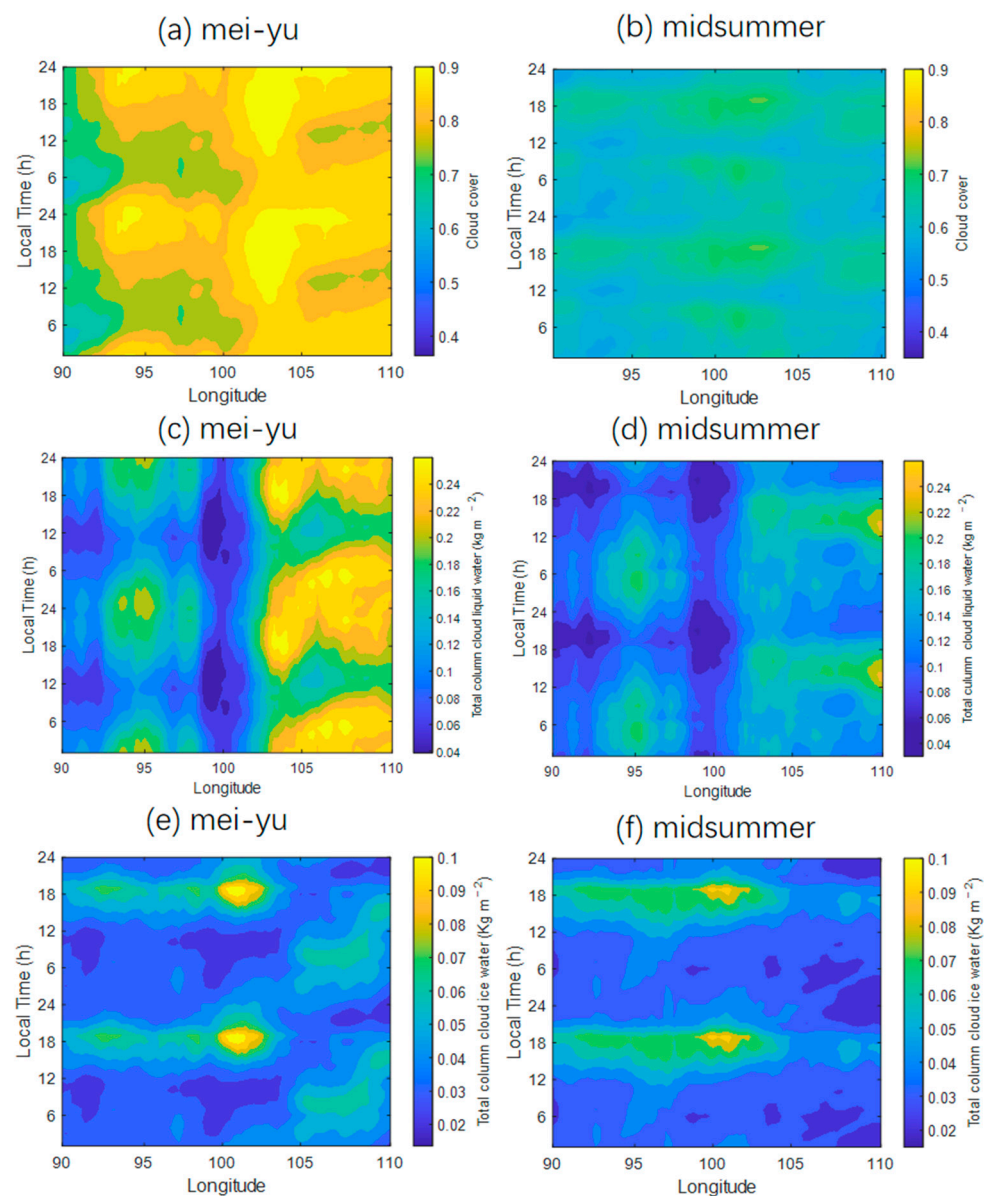


Figure 3. Diurnal variation in (a,b) cloud cover, (c,d) total column cloud liquid water content, and (e,f) cloud ice water content from ERA5 over the Tibetan Plateau and Sichuan Basin during the (a,c,e) mei-yu and (b,d,f) midsummer periods.

During the midsummer period, the diurnal variation in cloud cover (Figure 3b), LWC (Figure 3d), and IWC (Figure 3f) shows no propagation from the TP to SB. Over the TP, the diurnal maximum cloud cover and LWC lie within 1500–2100 LT and 0000–1200 LT, respectively, while the ranges for the diurnal minimum cloud cover and LWC are 1000–1500 LT and 1800–2100 LT. The cloud cover and LWC at the border of the SB and TP are smaller than those over the inner parts of the TP and SB. The cloud cover and LWC over the SB are larger than over the TP. Over both the TP and SB, the diurnal maximum IWC occurs in the mid-afternoon to early evening (1500–2100 LT) and reaches a diurnal minimum in the morning (2400–1200 LT).

The ratios of cloud LWC and IWC to total cloud water were separately calculated, and the results are presented in Figure 4. The results show that LWC accounts for more than 60% of total water during almost the entire diurnal cycle over the inner TP and SB during the mei-yu period, except for the period 1500–1800 LT at the edge of the SB and TP. The IWC accounts for more than 60% at around 1800 LT at the edge of the TP and SB, which is

related to the convergence rising motion over the slopes at the edge of the two regions. The proportions of LWC and IWC during midsummer are similar to those during the mei-yu period. However, there are two IWC centers during the midsummer period. One is in the period 1500–1800 LT at the edge of the SB and TP, and the other is located in the region 92° – 94° E during 1700–2000 LT, which is related to development of the westerly jet and southern water vapor transportation.

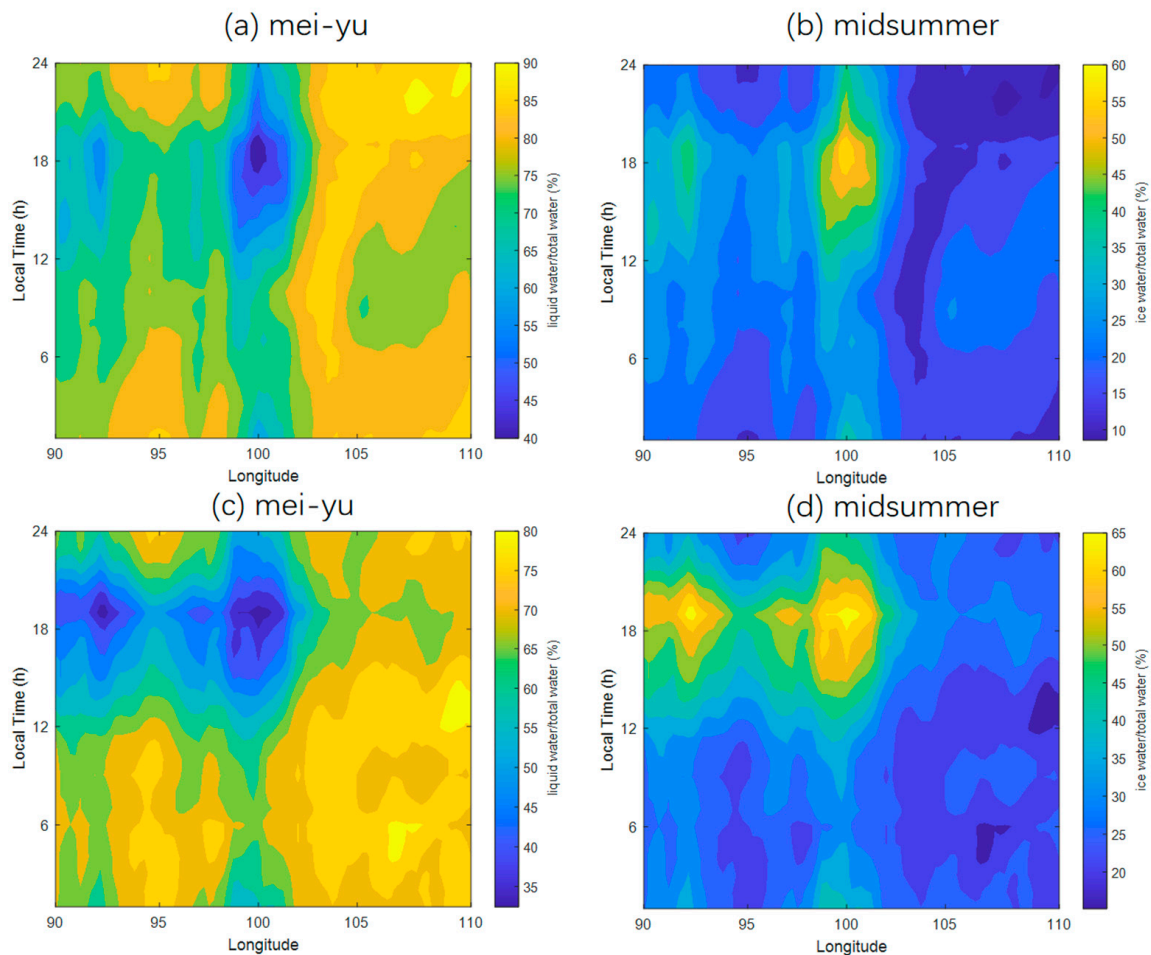


Figure 4. Ratio of cloud (a,c) liquid water and (b,d) ice water to total cloud water during the (a,b) mei-yu and (c,d) midsummer periods.

During the mei-yu period, the cloud LWC mainly distributes between the 900 hPa and 450 hPa level in the daytime and the 850–450 hPa level in the nighttime over the SB, while it mainly distributes between the 600 hPa and 450 hPa level in the daytime and the 600–400 hPa level in the nighttime over the TP (Figure 5a,b). The cloud LWC in the night is larger than that in the daytime over the SB. During the midsummer period, it is mainly similar to that over the SB and TP (Figure 5c,d) except that the cloud LWC during the midsummer period is smaller than that in the mei-yu period.

During the mei-yu period, the cloud IWC mainly distributes between the 450 hPa and 150 hPa level in the daytime and the 500–100 hPa level in the nighttime over the SB, while it mainly distributes between the 500 hPa and 180 hPa level in the daytime and the 450–100 hPa level in the nighttime over the TP (Figure 6a,b). The cloud IWC in the night is smaller than that in the daytime over the SB. During the midsummer period, it is mainly similar to that over the SB and TP except that the cloud IWC during the midsummer period is larger than that in the mei-yu period (Figure 6c,d). The cloud IWC in the daytime during the midsummer period mainly is concentrated over the edge of the SB and TP.

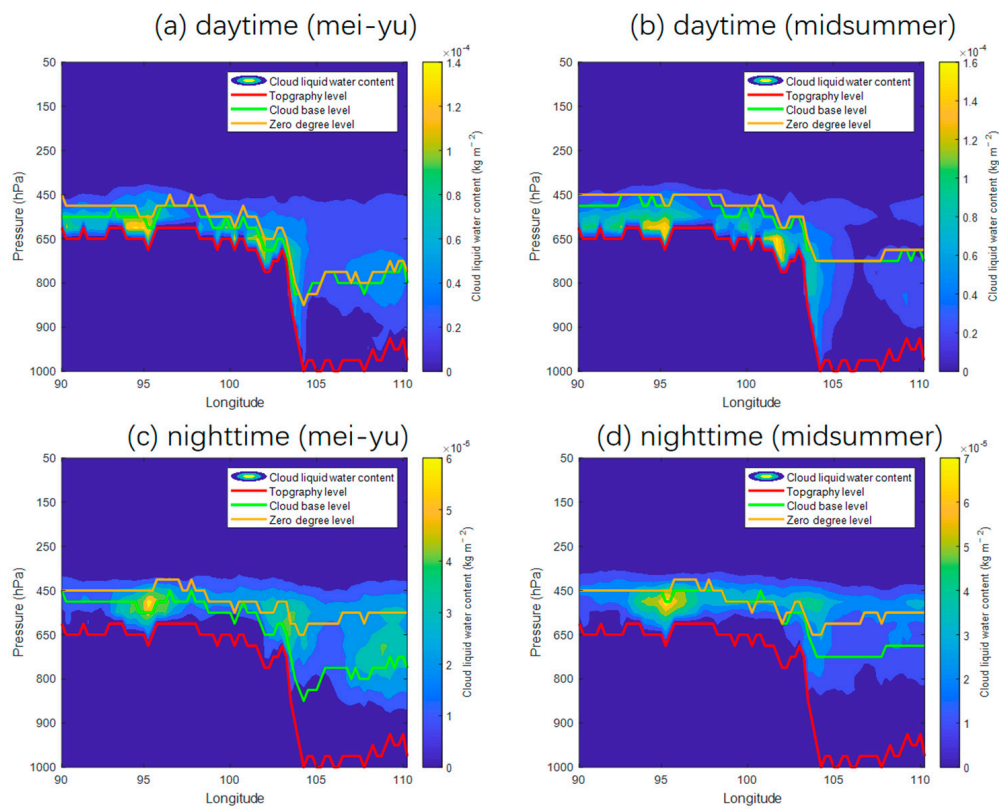


Figure 5. The pressure level of cloud liquid water content (shaded color), cloud base (green line), zero degree level (orange line), and the topography (red line) along with longitude during the (a,b) mei-yu and (c,d) midsummer periods during the (a,c) daytime and (b,d) nighttime.

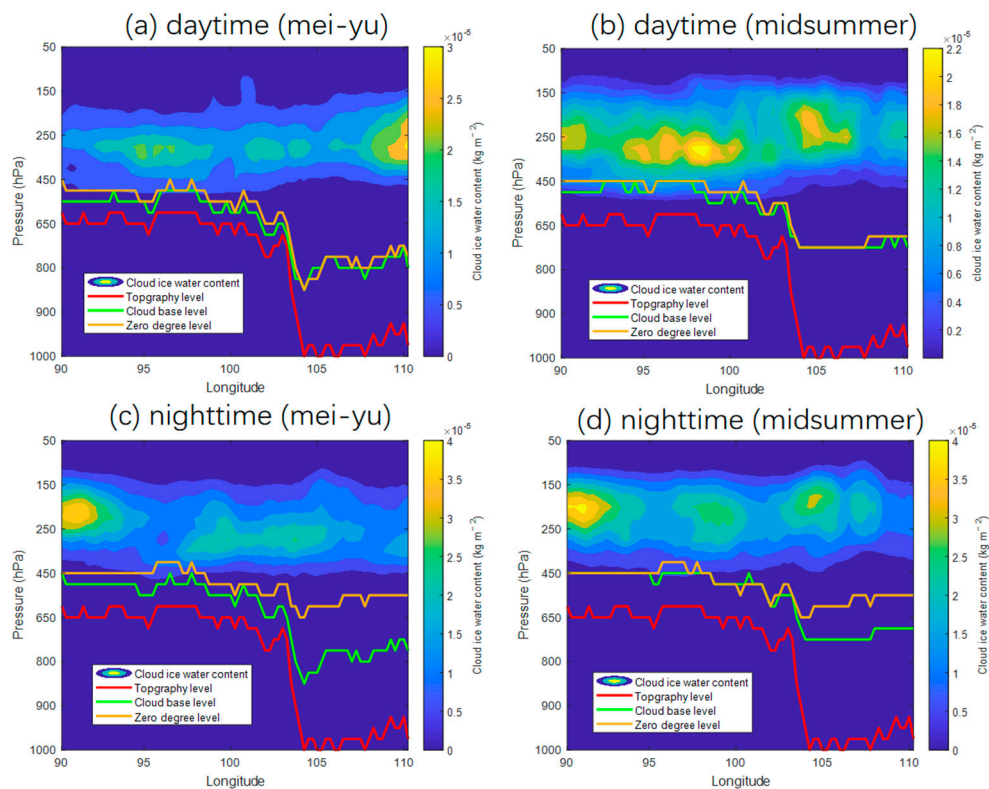


Figure 6. Similar with Figure 5, but for cloud ice water content.

The diurnal cycle of CBH AGL in ERA5 is presented in Figure 7. During the mei-yu period, the diurnal variation in CBH AGL shows propagation from west to east over the SB, while no propagation is apparent over the TP. The diurnal maximum CBH AGL over the TP is concentrated between 1500 LT and 2400 LT, while the diurnal minimum CBH AGL lies within 0900–1200 LT. The CBH AGL in the early evening is higher than that in the daytime over the SB, which is consistent with the nocturnal maximum precipitation. The CBH AGL over the SB is higher than that over the TP (Figure 7a). During the midsummer period, the diurnal variation in CBH AGL shows no propagation from the TP to SB. The diurnal maximum CBH AGL over the TP is concentrated between 2100 LT and 0300 LT, while the diurnal minimum lies within 0700–1500 LT. Over the SB, the diurnal maximum CBH AGL lies within the period 2100–0600 LT, while the diurnal minimum is within 1500–2100 LT (Figure 7b). The average CBH AGL observed by the cloud radar at Yushu, Naqu, and Linzhi is close to that in ERA5 (Figure S2). The maximum CBH AGL from ERA5 is in-phase with the observations averaged from the three sites during the mei-yu (Figure S2a) and midsummer (Figure S2b) periods over the TP.

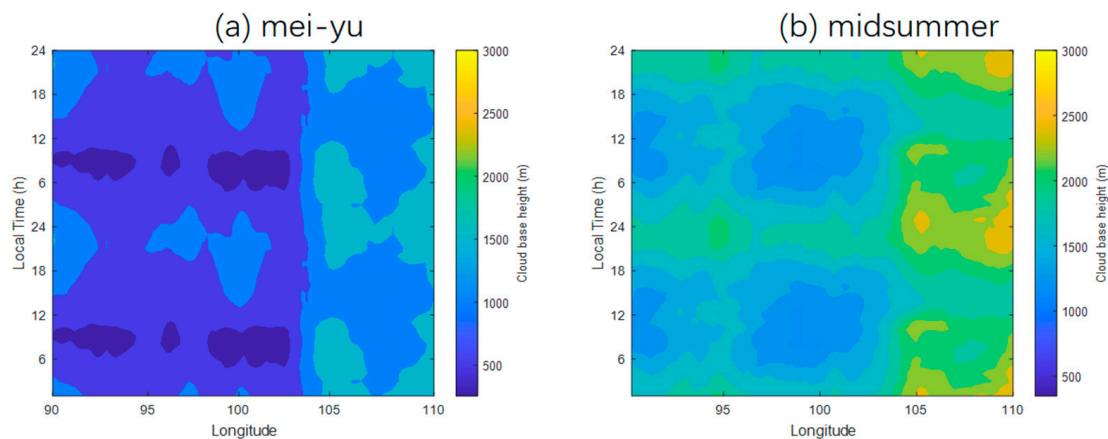


Figure 7. Diurnal variation in cloud base height from ERA5 over the Tibetan Plateau and Sichuan Basin during the (a) mei-yu and (b) midsummer periods.

The CBH AGL is compared with the zero degree level AGL in Figure 5. The zero degree level AGL is much higher than the CBH AGL over the TP and SB during the mei-yu period, while CBH AGL nears the zero degree level AGL over the TP during midsummer. The latter is related to the air temperature lapse rate, which is larger over the TP than the SB. The zero degree level MSL over the TP is higher than that over the SB. The thickness of cloud LWC over the SB is larger than that near the edge of the TP during the mei-yu and midsummer periods. The zero degree level MSL increases while the CBH remains stable with the increase in distance from the TP. However, super-cooled liquid water can exist down to $-40\text{ }^{\circ}\text{C}$.

4.2. Factors Influencing the Formation of Cloud over the TP and SB

During the mei-yu period, the diurnal variation in dewpoint spread shows no propagation from morning to night over the SB and TP (Figure 8a,b). As is well known, the dewpoint spread is mainly influenced by the solar radiation and surface heating. The diurnal maximum dewpoint spread is concentrated between 1500 LT and 2100 LT, and the diurnal minimum dewpoint spread lies within 0000–0900 LT in the region 90° – 100°E during mei-yu period (Figure 8a). During the midsummer period, the diurnal variation in dewpoint spread shows no propagation from the TP to SB. The diurnal maximum dewpoint spread is concentrated between 1500 LT and 2100 LT, while the range for the diurnal minimum is 0600–1000 LT (Figure 8b). The dewpoint spread over the SB is larger than that over the TP.

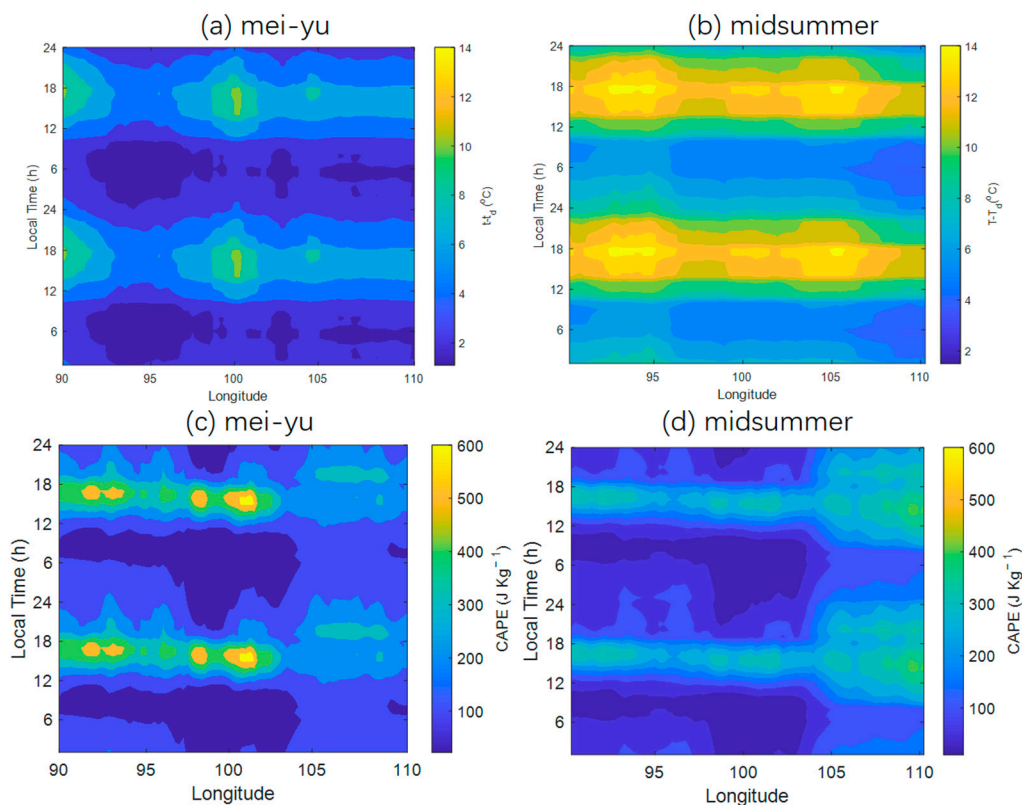


Figure 8. Diurnal variation in (a,b) dewpoint spread and (c,d) convective available potential energy (CAPE) from ERA5 over the Tibetan Plateau and Sichuan Basin during the (a,c) mei-yu and (b,d) midsummer periods.

A comparison of the dewpoint spread between the observation and ERA5 is given in Figure S3. Over both the TP and SB, the timing of the diurnal maximum dewpoint spread is similar to that in the observations during both the mei-yu and midsummer period. The dewpoint spread from ERA5 is larger than that in the observations, especially during the early evening. Some studies show that the dewpoint spread makes a profound contribution to the LCL (e.g., [43]). In this study, the CBH is close to the LCL during the summer period with large amounts of LWC during that same season (Table 2).

Table 2. Comparison of cloud base height (CBH) from ERA5 dataset and lifting condensation level (LCL) above ground level (AGL) during summer over the Tibetan Plateau (TP) and Sichuan Basin (SB).

	TP		SB	
	Mei-Yu	Midsummer	Mei-Yu	Midsummer
CBH AGL (m)	822	901	2556	2341
LCL AGL (m)	753	856	2468	2390

To investigate the effect of dewpoint spread on the CBH AGL, a correlation analysis between the two at each longitudinal grid point in ERA5 was carried out (Figure 9a). Over the TP, the correlation coefficient reaches up to 0.8 at the 5% significance level. However, it decreases at the edge of the TP and SB and becomes gradually negative, reaching a maximum negative value over the inner part of the SB. According to the above-mentioned results, CBH AGL propagates diurnally from the TP to SB, but the dewpoint spread does not. Therefore, the dewpoint spread makes a profound contribution to the CBH over the TP, but little contribution to the CBH AGL over the SB because of the stronger turbulence and lower air density over the TP than the SB [44].

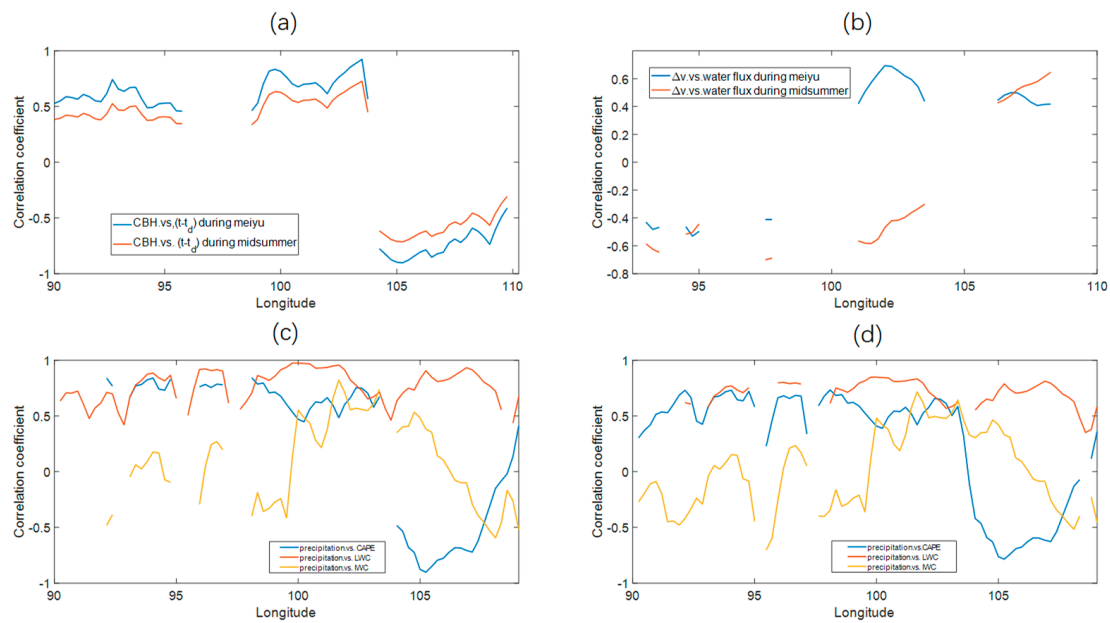


Figure 9. Correlation between (a) dewpoint spread and CBH and (b) water vapor flux and ΔV during the mei-yu (blue line) and midsummer (red line) periods. (c,d) Correlation of ΔV , CAPE, cloud LWC and IWC with precipitation rate during the (c) mei-yu and (d) midsummer periods.

From the spatial distribution of the water vapor flux, the transportation of water vapor can be seen to be mainly from the west (Figure 10), which is similar to the results of [45]. The water vapor flux decreases from the mei-yu period to the midsummer period, especially over the SB. This is related to the decreases in the mean zonal wind profile and low-level winds from the mei-yu to midsummer period.

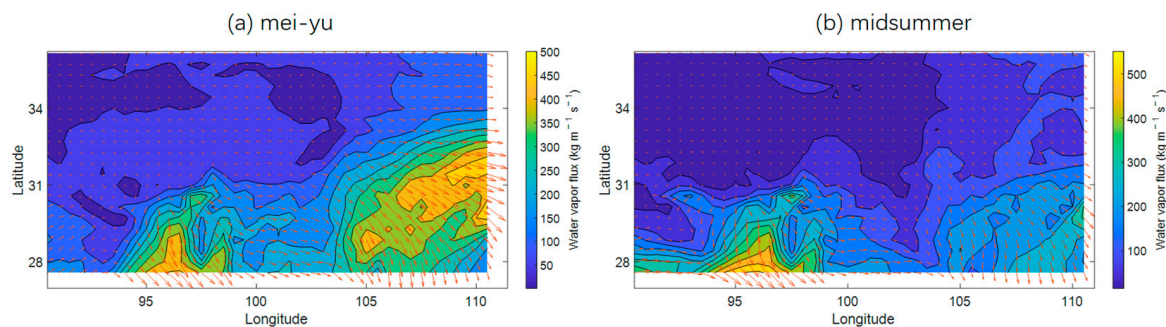


Figure 10. Integral of water vapor flux at 1800 LT from ERA5 over the (a) mei-yu and (b) midsummer periods.

To investigate the relationship between the total water vapor transportation and westerly wind, the difference in horizontal wind speed between 200 hPa and 500 hPa (ΔV) was calculated (Figure 11); that is, $\Delta V = [u(200) - u(500)]^2 + [v(200) - v(500)]^2$, where $u(200)$ and $v(200)$ refer to u -wind and v -wind at the 200 hPa level, respectively, and $u(500)$ and $v(500)$ refer to the same but at the 500 hPa level. Correlation analysis was carried out between the water vapor flux and ΔV . The ΔV over both the TP and SB decreases from the mei-yu to midsummer period, and the ΔV over the TP is larger than that over the SB during both periods. The ΔV correlates positively with water vapor transportation at the 5% significance level over the TP and SB, and the correlation coefficient over the TP is smaller than that over the SB during the mei-yu and midsummer periods (Figure 9b). The ΔV has a profound impact on the transportation of water vapor over the SB. The correlation coefficient decreases dramatically from the mei-yu to midsummer period in the region of 90° – 100° E where the steep slopes and SB are situated.

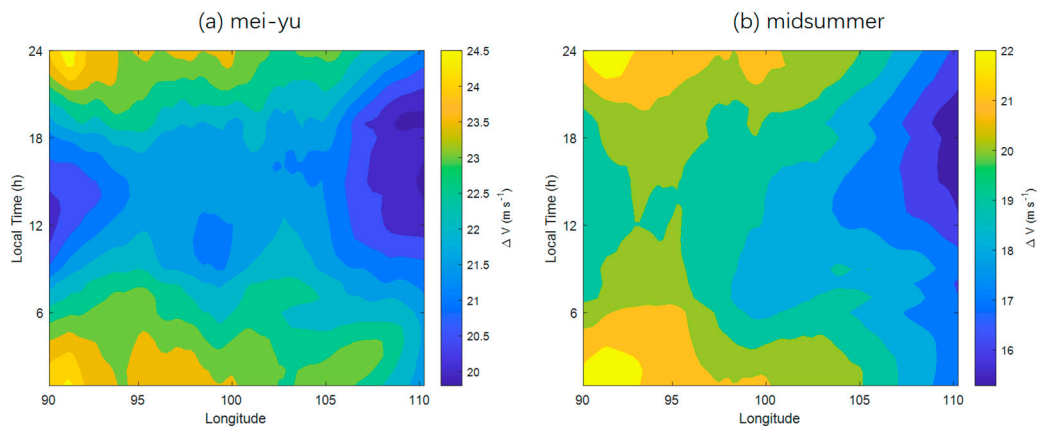


Figure 11. Diurnal variation in ΔV during the (a) mei-yu and (b) midsummer periods.

4.3. Factors Influencing the Formation of Precipitation over the TP and SB

To investigate the factors influencing the precipitation, the diurnal cycle of CAPE is shown in Figure 8c,d. During the mei-yu period, CAPE shows no propagation over the TP and SB (Figure 8c). The diurnal maximum CAPE occurs in the late afternoon (1500–1900 LT) and early evening (1900–2100 LT) over the TP and SB during the mei-yu period, and the diurnal minimum occurs in the morning (0600–1000 LT). The CAPE over the TP is larger than that over the SB (Figure 8c), which is different from the precipitation and cloud LWC. During the midsummer period, CAPE shows no diurnal propagation over the TP and SB (Figure 8d). The diurnal maximum and minimum CAPE values during the mei-yu period are similar to those during the midsummer period. CAPE is related to the maximum potential vertical velocity of air within an updraft, so higher values of CAPE are an indicator of precipitation.

To investigate the influence of diurnal variation in CAPE, cloud LWC and IWC on precipitation, correlation analysis was performed. During the mei-yu period, the correlation coefficient between CAPE and precipitation over the TP is larger than that over the SB. The correlation coefficient reaches a maximum (0.8) at the edge of the TP and SB at the 5% significance level (Figure 9c). The correlation coefficient between CAPE and precipitation during the midsummer period is smaller than that during the mei-yu period (Figure 9d). These results indicate that CAPE has a larger impact on precipitation over the TP than over the SB.

The correlation coefficient between cloud IWC and precipitation over the TP and SB is larger than 0.7, with a significance level of 5%, during the mei-yu period. The correlation coefficient between cloud LWC and precipitation over the SB during the midsummer period (Figure 9d) is smaller than that during the mei-yu period, which decreases with longitude from west to east due to the diurnal propagation of LWC and precipitation (Figure 9c), while the opposite is the case for cloud IWC. However, the correlation between the cloud IWC and precipitation over the edge of the TP and SB is better than over the inner parts of the TP and SB due to the convergence rising motion over the slopes. The above results indicate that the cloud LWC makes a large contribution to precipitation over the SB. The precipitation over the edge of the TP and SB (i.e., the steep downstream slopes) is influenced by the cloud IWC.

5. Conclusions

The diurnal variations in precipitation in the HE Satellite Rainfall Estimates and cloud parameters (CBH AGL, cloud cover, cloud LWC and IWC, and dewpoint spread) in the ERA5 dataset were analyzed over the TP and SB. Results show that the precipitation and cloud parameters show diurnal propagation from morning to night over the SB during the mei-yu period, while no such diurnal propagation is apparent over the TP during both the mei-yu and midsummer periods. The precipitation, cloud LWC and IWC, and cloud cover

over the TP are smaller than over the SB. The dewpoint spread over the TP is larger than over the SB. The diurnal maximum precipitation and cloud LWC and IWC are concentrated in the early evening, while the diurnal minima occur in the morning.

The precipitation from the HE Satellite is larger than that in the observations. Over the SB, the maximum precipitation from the HE Satellite is 3 h ahead of observations. The result for the PF number percentage is similar to that of the precipitation amount. During both the mei-yu and midsummer period, the cloud LWC from ERA5 at night is larger than that in the daytime. Cloud LWC accounts for more than 60% of total water during almost the entire diurnal cycle over the inner parts of the TP and SB during the mei-yu period except for late afternoon at the edge of the SB and TP. The cloud IWC accounts for more than 60% during early evening at the edge of the TP and SB.

The CBH AGL, LCL AGL, and zero degree level AGL are almost equal over the TP during the summer period. The zero degree level AGL over the SB is higher than that over the TP because the air temperature lapse rate over the TP is larger than that over the SB. The thickness of the LWC over the SB is larger than that over the TP. The dewpoint spread makes a profound contribution to the CBH AGL over the TP but little contribution to the CBH AGL over the SB because of the stronger turbulence and lower air density over the TP. CAPE has a larger impact on precipitation over the TP than over the SB. The cloud LWC makes a large contribution to the precipitation over the SB, which is related to the mean zonal wind profile and diurnal cycle of low-level winds. The precipitation over the edge of the TP and SB (i.e., the steep downstream slopes) is influenced by the cloud IWC owing to the convergence rising motion over the slopes.

Although the distribution of cloud LWC and IWC over the TP and SB was obtained in this study, the distribution of supercooled water and ice level over the edge of TP and SB is still unclear and needs to be investigated. In addition, the results of ERA5 data were uncertainty limited by the resolution of ERA5 data, especially concerning quite an extreme region. The current cloud radar sites are very sparse, making it impossible directly to observe the cloud microphysical parameter data over the entire TP and SB. In the future, the accuracy of the reanalysis dataset and observations over the TP and SB at night should be improved. More cloud radar observations at different locations over the TP and SB are needed in the future. The phase of water within cloud needs to be studied using different kinds of observational and model data.

Supplementary Materials: The following supporting information can be downloaded at <https://www.mdpi.com/article/10.3390/rs14112711/s1>: Table S1: The information of ground meteorological observation sites of China Meteorological Administration; Table S2: The information of radiosonde station of China Meteorological Administration; Figure S1: The precipitation from Hydro Estimator satellite estimates (blue line) and ground observations (red line) during (a,b) mei-yu and (c,d) midsummer period over the (a,c) Tibetan Plateau and (b,d) Sichuan Basin. Blue shaded area is the standard error of precipitation from Hydro Estimator satellite estimates, and red shaded area is the standard error of precipitation from ground observations. The percentage of precipitation feature during (e,f) mei-yu and (g,h) midsummer period over the (e,g) Tibetan Plateau and (f,h) Sichuan Basin and their error bar. Blue shaded area is the standard error of the percentage of precipitation feature from Hydro Estimator satellite estimates, and red shaded area is the standard error of percentage of precipitation feature from ground observations; Figure S2: The comparison of cloud base height from ERA5 dataset (blue line) and cloud radar observations (red line) and their standard error (blue shaded area for ERA5 and red shaded area for observations) during the (a) mei-yu and (b) midsummer period; Figure S3: The comparison of dew point spread from the ERA5 dataset (blue line) and ground observations (red line) and their standard error (blue shaded area for ERA5 dataset, and red shaded area for observations) during the (a,b) mei-yu and (c,d) midsummer period over the (a,c) Tibetan Plateau and (b,d) Sichuan Basin.

Author Contributions: Conceptualization, Y.L.; methods, B.C.; software, B.C.; validation, Y.L.; writing—original draft preparation, B.C.; writing—review and editing, X.Y.; visualization, B.L.; supervision, J.W.; project administration, X.Y.; funding acquisition, X.Y. All authors have read and agreed to the published version of the manuscript.

Funding: This research was funded by the National Science Foundation of China (NSFC) (41975130, 42175174), Strategic Priority Research Program of Chinese Academy of Sciences (XDA20050102), the Second Tibetan Plateau Scientific Expedition and Research (STEP) program (2019QZKK0102), the Research Foundation of Chengdu University of Information Technology (KYTZ201810), and the Project of Science and Technology Plan of Sichuan (2019YJ0408).

Data Availability Statement: The ERA5 data employed in this study are available from <https://www.ecmwf.int/en/forecasts/datasets/reanalysis-datasets/era5> (accessed on 1 January 2022). The observational data are available from the third Tibetan Plateau Atmospheric Experiment (TIPEX3; <https://data.cma.cn/site/article/id/28986.html> (accessed on 1 January 2022)).

Conflicts of Interest: The authors declare no conflict of interest.

Abbreviations

TP	Tibetan Plateau
SB	Sichuan Basin
EASM	East Asian summer monsoon
ECMWF	European Centre for Medium-Range Weather Forecasts
ERA5	ECMWF Reanalysis v5
PERSIANN-CDR	Precipitation Estimation from Remotely Sensed Information using Artificial Neural Networks-Climate Data Record
IMERG	Integrated Multi-satellite Retrievals for GPM
TMPA	Tropical Rainfall Measuring Mission (TRMM) Multisatellite Precipitation Analysis
CMORPH	Climate Prediction Center Morphing technique
HE	Hydro-Estimator Satellite Rainfall Estimates
LT	Local time
UTC	Coordinated Universal Time
PF	Precipitation Feature
AGL	Above ground level
MSL	Mean sea level
CBH	Cloud base height
LCL	Lifting condensation level
CAPE	Convective available potential energy
LWC	Cloud liquid water content
IWC	Cloud ice water content

References

- Xu, X.; Lu, C.; Shi, X.; Gao, S. World water tower: An atmospheric perspective. *Geophys. Res. Lett.* **2008**, *35*, L20815. [[CrossRef](#)]
- Fu, Y.; Liu, G.; Wu, G.; Yu, R.; Xu, Y.; Wang, Y.; Li, R.; Liu, Q. Tower mast of precipitation over the central Tibetan Plateau summer. *Geophys. Res. Lett.* **2006**, *33*, L05802. [[CrossRef](#)]
- Boos, W.R.; Kuang, Z. Dominant control of the South Asian monsoon by orographic insulation versus plateau heating. *Nature* **2010**, *463*, 218–222. [[CrossRef](#)] [[PubMed](#)]
- Fu, Y.; Ma, Y.; Zhong, L.; Yang, Y.; Guo, X.; Wang, C.; Xu, X.; Yang, K.; Xu, X.; Liu, L.; et al. Land surface processes and summer cloud-precipitation characteristics in the Tibetan Plateau and their effects on downstream weather: A review and perspective. *Natl. Sci. Rev.* **2020**, *7*, 500–515. [[CrossRef](#)] [[PubMed](#)]
- Kukulies, J.; Chen, D.; Curio, J. The role of mesoscale convective systems in precipitation in the Tibetan Plateau region. *J. Geophys. Res. Atmos.* **2021**, *126*, e2021JD035279. [[CrossRef](#)]
- Barton, E.; Taylor, C.; Klein, C.; Harris, P.; Meng, X. Observed soil moisture impact on strong convection over mountainous Tibetan Plateau. *J. Hydrometeorol.* **2021**, *22*, 561–572. [[CrossRef](#)]
- Houze, R.A.; Wilton, D.C.; Smull, B.F. Monsoon convection in the Himalayan region as seen by the TRMM precipitation radar. *Q.J.R. Meteorol. Soc.* **2007**, *133*, 1389–1411. [[CrossRef](#)]
- Zhao, P.; Xu, X.; Chen, F.; Guo, X.; Zheng, X.; Liu, L.; Hong, Y.; Li, Y.; La, Z.; Peng, H. The Third Atmospheric Scientific Experiment for understanding the earth-atmosphere coupled system over the Tibetan Plateau and its effects. *Bull. Am. Meteorol. Soc.* **2017**, *99*, 757–776. [[CrossRef](#)]
- Bai, A.J.; Liu, C.; Liu, X. Diurnal variation of summer rainfall over the Tibetan Plateau and its neighboring regions revealed by TRMM multi-satellite precipitation analysis. *Chin. J. Atmos. Sci.* **2008**, *51*, 518–529. [[CrossRef](#)]
- Feng, J.; Liu, L.; Wang, Z. The statistic characteristics of radar echo and precipitation and some thermodynamic variables at Naqu in Qinghai-Xizang Plateau. *Plateau Meteorol.* **2002**, *21*, 368–374. (In Chinese)

11. Zhao, P.; Xiao, H.; Liu, J.; Zhou, Y. Precipitation efficiency of cloud and its influencing factors over the Tibetan plateau. *Int. J. Climatol.* **2022**, *42*, 416–434. [[CrossRef](#)]
12. Tao, S.; Chen, L. A review of recent research on the East Asian summer monsoon in China. In *Monsoon Meteorology*; Chang, C.P., Krishnamurti, T.N., Eds.; Oxford University Press: Oxford, UK, 1987; pp. 60–92.
13. Ding, Y. Summer monsoon rainfalls in China. *J. Meteor. Soc. Jpn.* **1992**, *70*, 373–396. [[CrossRef](#)]
14. Chen, G. Large-scale circulations associated with the East Asian summer monsoon and the mei-yu over South China and Taiwan. *J. Meteor. Soc. Jpn.* **1994**, *72*, 959–983. [[CrossRef](#)]
15. Ding, Y.; Chan, J.C.-L. The East Asian summer monsoon: An overview. *Meteor. Atmos. Phys.* **2005**, *89*, 117–142.
16. Chen, G. Research on the phenomena of Meiyu during the past quarter century: An overview. In *The East Asian Monsoon*; Chang, C.-P., Ed.; World Scientific: Singapore, 2004; pp. 357–403.
17. Liu, L.; Zheng, J.; Zheng, R.; Cui, Z.; Hu, Z.; Wu, S.; Dai, G.; Wu, Y. Comprehensive radar observations of clouds and precipitation over the Tibetan Plateau and preliminary analysis of cloud properties. *J. Meteorol. Res.* **2015**, *29*, 546–561. [[CrossRef](#)]
18. Mei, Y.; Hu, Z.; Huang, X. A study of convective clouds in the Tibetan Plateau based on dual polarimetric radar observations. *Acta Meteor Sin.* **2018**, *76*, 1014–1028. [[CrossRef](#)]
19. Liu, L.; Feng, J.; Chu, R.; Zhou, Y.; Ueno, K. The diurnal variation of precipitation in monsoon season in the Tibetan Plateau. *Adv. Atmos. Sci.* **2002**, *19*, 365–378. [[CrossRef](#)]
20. Fujinami, H.; Yasunari, T. The seasonal and intraseasonal variability of diurnal cloud activity over the Tibetan Plateau. *J. Meteor. Soc. Jpn.* **2001**, *79*, 1207–1227. [[CrossRef](#)]
21. Ji, X.L.; Wu, H.M.; Huang, A.N.; Zhao, W.; Yang, W. Characteristics of the precipitation diurnal variation over Qinghai-Tibetan Plateau in summer. *Plateau Meteor.* **2017**, *36*, 1188–1200. (In Chinese)
22. Zhao, C.; Liu, L.; Wang, Q.; Qiu, Y.; Wang, Y.; Wu, X. MMCR-based characteristic properties of non-precipitating cloud liquid droplets at Naqu site over Tibetan Plateau in July 2014. *Atmos. Res.* **2017**, *190*, 68–76. [[CrossRef](#)]
23. Xu, W.; Zipser, E.J. Diurnal variations of precipitation, deep convection, and lightning over and east of the eastern Tibetan Plateau. *J. Clim.* **2011**, *24*, 448–465. [[CrossRef](#)]
24. Fu, Y.; Pan, X.; Xian, T.; Liu, G.; Zhong, L.; Liu, Q.; Ma, M. Precipitation characteristics over the steep slope of the Himalayas in rainy season observed by TRMM PR and VIRS. *Clim. Dyn.* **2018**, *51*, 1971–1989. [[CrossRef](#)]
25. Gong, Y.F.; Ji, L.R.; Duan, T.Y. Precipitation character of rainy season of Qinghai-Xizang Plateau and onset over East Asia monsoon. *Plateau Meteor.* **2004**, *23*, 313–322. (In Chinese)
26. Chen, G.; Sha, W.; Iwasaki, T. Diurnal variation of precipitation over southeastern China: 2. Impact of the diurnal monsoon variability. *J. Geophys. Res.* **2009**, *114*, D21105. [[CrossRef](#)]
27. Yu, R.; Li, J.; Chen, H.; Yuan, W. Progress in studies of the precipitation diurnal variation over contiguous China. *Acta Meteorol. Sin.* **2014**, *72*, 948–968. [[CrossRef](#)]
28. Sorooshian, S.; Hsu, K.L.; Gao, X.; Gupta, H.V.; Imam, B.; Braithwaite, D. Evaluation of PERSIANN system satellite-based estimates of tropical rainfall. *Bull. Am. Meteorol. Soc.* **2000**, *81*, 2035–2046. [[CrossRef](#)]
29. Huffman, G.J.; Bolvin, D.T.; Nelkin, E.J. Integrated Multi-satellite Retrievals for GPM (IMERG) Technical Documentation. NASA/GSFC Code 612; 2015. Available online: http://pmm.nasa.gov/sites/default/files/document_files/IMERG_doc.pdf (accessed on 16 September 2019).
30. Huffman, G.J.; Bolvin, D.T.; Nelkin, E.J.; Wolff, D.B.; Adler, R.F.; Gu, G.; Hong, Y.; Bowman, K.P.; Stocker, E.F. The TRMM multisatellite precipitation analysis (TMPA): Quasi-global, multiyear, combined-sensor precipitation estimates at fine scales. *J. Hydrometeorol.* **2007**, *8*, 38–55. [[CrossRef](#)]
31. Joyce, R.J.; Janowiak, J.E.; Arkin, P.A.; Xie, P. CMORPH: A method that produces global precipitation estimates from passive microwave and infrared data at high spatial and temporal resolution. *J. Hydrometeorol.* **2004**, *5*, 487–503. [[CrossRef](#)]
32. Scofield, R.A.; Kuligowski, R.J. Status and outlook of operational satellite precipitation algorithms for extreme-precipitation events. *Mon. Wea. Rev.* **2003**, *18*, 1037–1051. [[CrossRef](#)]
33. Hobouchian, M.P.; Salio, P.; Skabar, Y.G.; Daniel, V.; Rene, G. Assessment of satellite precipitation estimates over the slopes of the subtropical Andes. *Atmos. Res.* **2017**, *190*, 43–54. [[CrossRef](#)]
34. Yucel, I.; Kuligowski, R.J.; Gochis, D.J. Evaluating the hydro-estimator satellite rainfall algorithm over a mountainous region. *Int. J. Remote Sens.* **2011**, *32*, 7315–7342. [[CrossRef](#)]
35. Liu, J. Analysis on cloud microphysical property over Qinghai-Xizang Plateau using satellite data. *Plateau Meteor.* **2013**, *32*, 38–45. (In Chinese)
36. Cadeddu, M.; Liljegren, J.; Turner, D. The atmospheric radiation measurement (ARM) program network of microwave radiometers: Instrumentation, data, and retrievals. *Atmos. Meas. Tech.* **2013**, *6*, 2359–2372. [[CrossRef](#)]
37. Zhao, C.; Xie, S.; Klein, S. Toward understanding of differences in current cloud retrievals of ARM ground-based measurements. *J. Geophys. Res.* **2012**, *117*, D10206. [[CrossRef](#)]
38. Guo, J.P.; Zhang, J.; Yang, K.; Liao, H.; Zhang, S.D.; Huang, K.M.; Lv, Y.M.; Shao, J.; Yu, T.; Tong, B.; et al. Investigation of near-global daytime boundary layer height using high-resolution radiosondes: First results and comparison with ERA5, MERRA-2, JRA-55, and NCEP-2 reanalyses. *Atmos. Chem. Phys.* **2021**, *21*, 17079–17097. [[CrossRef](#)]
39. Cao, B.J.; Lyu, S.H.; Zhang, Y.; Yang, X.; Li, B.; Li, M. Factors influencing diurnal variations of cloud and precipitation in the Yushu area of the Tibetan Plateau. *J. Meteor. Res.* **2022**, *36*, 311–325. [[CrossRef](#)]

40. Chen, M.; Chen, M.X.; Fan, S.Y. The real-time radar radial velocity 3DVar assimilation experiments for application to an operational forecast model in North China. *Acta Meteor. Sinica* **2014**, *72*, 658–677. (In Chinese) [[CrossRef](#)]
41. Wang, Y.; Yang, Y.; Wang, C.H. Improving forecasting of strong convection by assimilating cloud-to-ground lightning data using the physical initialization method. *Atmos. Res.* **2014**, *150*, 31–41. [[CrossRef](#)]
42. Zhang, Y.; Xue, M.; Zhu, K.; Zhou, B. What is the main cause of diurnal variation and nocturnal peak of summer precipitation in Sichuan Basin, China? The key role of boundary layer low-level jet inertial oscillations. *J. Geophys. Res. Atmos.* **2019**, *124*, 2643–2664. [[CrossRef](#)]
43. Craven, J.P.; Jewell, R.E.; Brooks, H.E. Comparison between observed convective cloud-base heights and lifting condensation level for two different lifted parcels. *Wea. Forecast* **2002**, *17*, 885–890. [[CrossRef](#)]
44. Wang, Y.; Zeng, X.; Xu, X.; Welty, J.; Lenschow, D.H.; Zhou, M.; Zhao, Y. Why are there more summer afternoon low clouds over the Tibetan Plateau compared to eastern China? *Geophys. Res. Lett.* **2020**, *47*, e2020GL089665. [[CrossRef](#)]
45. Wu, G.X.; Duan, A.; Liu, Y.; Mao, J.; Ren, R.; Bao, Q.; He, B.; Liu, B.; Hu, W. Tibetan Plateau climate dynamics: Recent research progress and outlook. *Natl. Sci. Rev.* **2015**, *2*, 110–116. [[CrossRef](#)]